

During the tunnel construction phases, the time increment used for the time-dependent analysis is automatically managed by the ANSYS solver. The latter makes use of a semi-implicit scheme for the viscoplasticity solution, together with an automatic time stepping algorithm [34] in which the time step is defined as a fraction of time t_p for the phases of longitudinal tunnel excavation and as a fraction of t_{pg} for the phases of transverse gallery excavation. Furthermore, distinct time steps are considered for the time-dependent analysis during tunnelling process and post-excavation stage. After complete tunnel construction phases, the analysis is carried out for a period of about 3000 days to assess the time evolving deformation as well as long-term viscous effects on the final equilibrium of the tunnel structure. At that respect and in anticipation of the numerical results of the subsequent sections, the characteristic viscoplastic relaxation time [35] is equal to $\bar{\tau} = \eta f_0 / E$, which is close to 30 days for model data of Table 2.

6. Preliminary numerical simulations and computational model verification

This section is aimed at applying the computational modeling to simulate deformation and stress in two academic twin tunnels configurations. The numerical results provided in these illustrative applications may be viewed as preliminary verifications of the F.E formulation. The first application refers to unlined twin tunnels excavated in an elastic rock mass, whereas the second application addresses the situation of unlined twin tunnels excavated in an elastoplastic medium.

6.1. Unlined twin tunnels in elastic medium

In the context of plane strain conditions, Guo et al. [6] addressed the configuration of deep twin tunnels excavated in a homogeneous elastic medium in which prevails a hydrostatic initial stress distribution. The authors formulated approximate analytical solutions for the stress distribution establishing far behind the face, which are induced in the rock mass by the excavation of two parallel circular tunnels. The model geometry of the twin circular tunnels as well as the loading associated with initial stress (where $\sigma_h = \sigma_v$) are displayed in Fig. 12.

Simulation of the problem has been addressed by means of the 3D finite element model and the numerical results obtained for the stress distribution far behind the faces of the twin tunnel shall be compared to the analytical stress solution derived by Guo et al. [6] in the framework of plane strain conditions. The simulations have been performed taking advantage of symmetry with respect to the midplane between twin tunnels and considering the following model data: tunnel radius $R_t = 4$ m, rock Young modulus $E = 500$ MPa and Poisson ratio $\nu = 0.23$, isotropic initial stresses of $\sigma_v = \sigma_h = 2.2$ MPa.

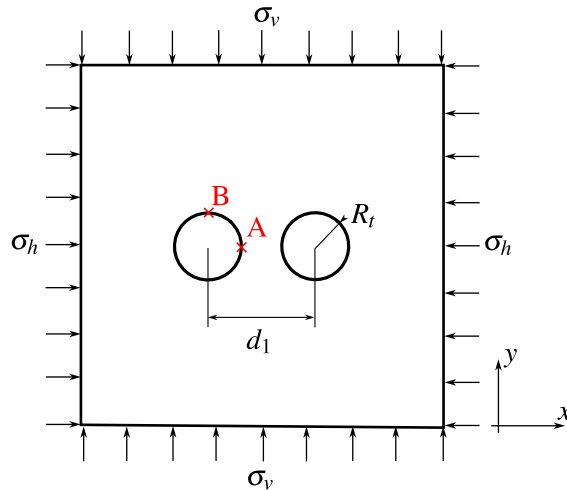


Figure 12: Geometry model and loading mode of the twin circular tunnels studied in Guo et al. [6].

Denoting by u_y the displacement component following the y -axis, Fig. 13 displays the convergence curves $U_B = -u_y(B)/R_t$ that characterize the inward movement at the tunnel roof $B(x = 0, y = R_t, z)$ as a function of normalized longitudinal distance to the facing. Several values of normalized distances between the twin tunnels axes $d_1/2R_t$ have been investigated, and the configuration of single tunnel may be viewed as the limiting case $d_1/2R_t \gg 1$.

It is recalled that in the latter configuration, the convergence far from the tunnel face that is obtained from an elastic analysis reads $U = \sigma_p(1 + \nu)/E$. As expected, this figure indicates that the closer the longitudinal tunnels, the greater the convergence at the roof.

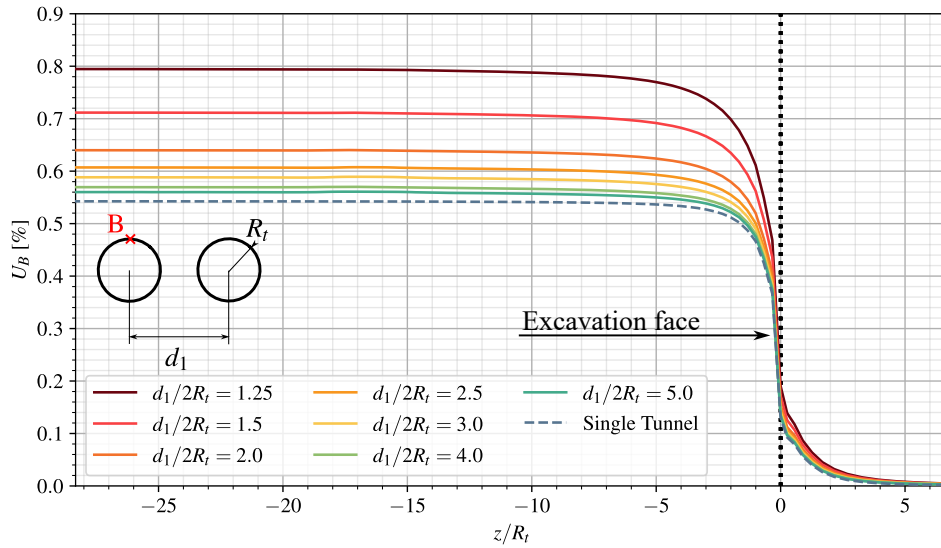


Figure 13: Convergence profiles in the tunnel roof (point B).

The tunnel deformation anisotropy induced by the twin tunnels proximity is illustrated in Fig. 14, which plots the ratio $U_B/U_A = u_y(B)/u_x(A)$ between the vertical displacement u_y at the roof B and the horizontal displacement u_x at the side wall A ($x = R_t, y = 0, z$). The results refer to a tunnel section located far behind the facing at normalized distance $z/R_t = -25$. They emphasize the significant tunnel ovalization induced by the proximity of twin tunnel as the distance $d_1/2R_t$ decreases.

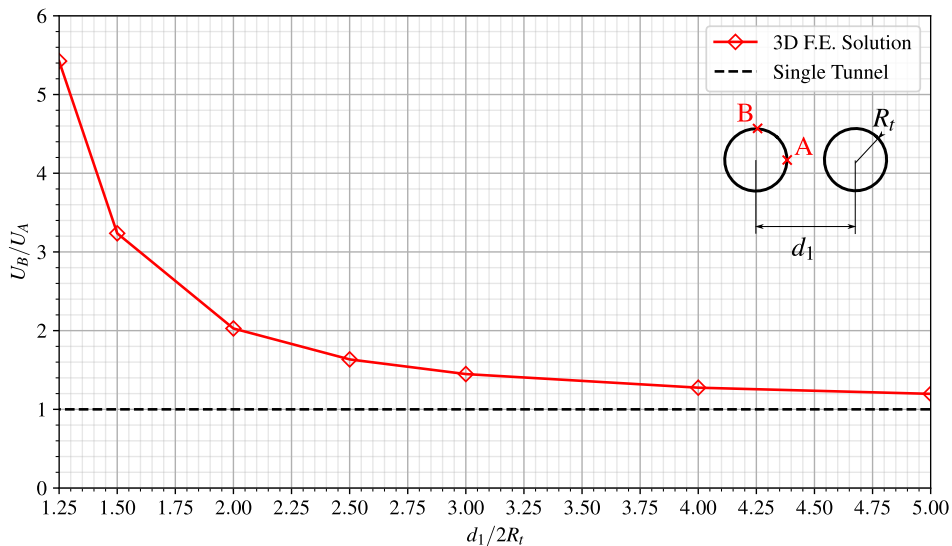


Figure 14: Illustration of the tunnel wall deformation anisotropy induced by twin tunnels proximity.

The stress distribution prevailing far from the facing that were obtained from the 3D numerical simulations are compared in Fig. 15 to the stress solutions derived analytically and numerically in Guo et al. [6]. In this figure, the tangential stress concentration factor σ_{yy}/σ_v computed at the side wall A is plotted for several values of the normalized twin tunnels distance. The results of the theoretical solution to a plate containing two circular holes of equal size presented in Ling et al. [37] are also reported in Fig. 15. It is observed that the results of the 3D finite element simulations correspond to a tunnel section located at normalized distance $z/R_t = -25$ from the facing, which is considered sufficient for the plane strain conditions to establish. Interestingly, the tangential stress concentration obtained for a deep single tunnel under plane strain condition simply reads $\sigma_{yy}/\sigma_v = 2$. Although the overall agreement observed between the different predictions, it appears from the comparison that the approximate analytical stress solution provided in [6] slightly overestimates the tangential stress computed at point A as the value of distance $d_1/2R_t$ increases.

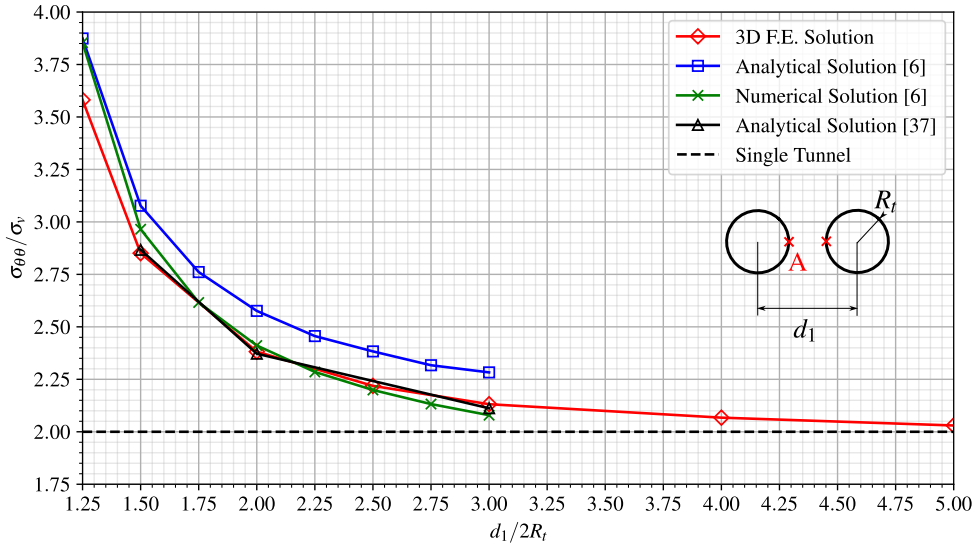


Figure 15: Tangential stress concentration factor at the side wall A versus twin tunnels distance $d_1/2R_t$.

Finally, Fig. 16 displays the distribution of tangential (orthoradial) stress $\sigma_{\theta\theta}$ around the tunnel boundary $\{r = R_t, 0 \leq \theta \leq \pi\}$ considering $d_1/2R_t = 1.5$. The predictions of stress component $\sigma_{\theta\theta}$ obtained from the 3D finite element simulations far behind the facing are shown together with the strain plane solutions derived analytically in [6], emphasizing the ability of the computational model to accurately capture the effect of tunnels proximity on stress distribution.

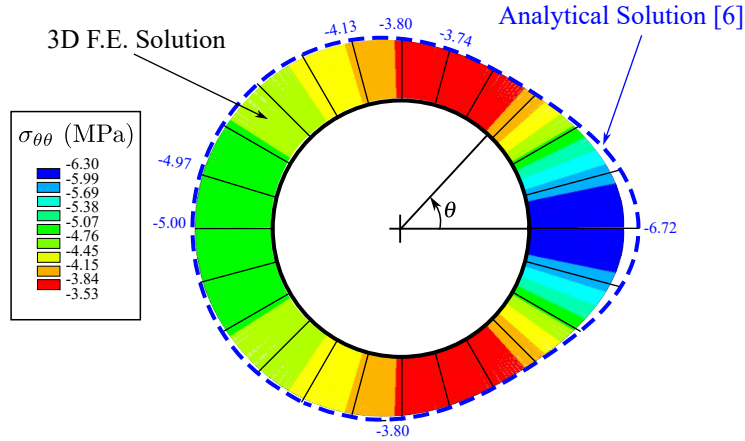


Figure 16: Distribution of tangential stress $\sigma_{\theta\theta}$ around the tunnel wall prevailing far behind the facing (twin tunnels distance $d_1/2R_t = 1.5$).

Keeping in mind it addresses only an academic configuration, the results provided in this section may be viewed as a first preliminary verification of the accuracy of the computational model formulated for the mechanical interaction in deep twin tunnels.

6.2. Unlined twin tunnels in elastoplastic medium

In the context of plane strain conditions, Ma et al. [9] developed an approximate analytical solution for the stresses and the plastic zone boundary around deep twin circular tunnels excavated in a homogeneous elastoplastic medium. The geometric model and initial stress state are the same as those shown in Fig. 12. However, this model does not assume necessarily equal initial stresses, and the initial stress along the tunnel axis is assumed as the middle stress, i.e., $\sigma_{zz} = (\sigma_v + \sigma_h)/2$. For the constitutive model, the authors considered perfectly plastic Mohr-Coulomb criterion with associated plastic flow rule. In this analytical solution, it is assumed that the plastic zones around each tunnel are isolated from each other and completely surround each tunnel.

Denoting by u_y the displacement component along the y-axis, Fig. 17 displays the convergence curves $U_B = -u_y(B)/R_t$, that characterize the inward movement at the tunnel roof $B(x = 0, y = R_t, z)$ as a function of normalized longitudinal distance to the excavation face, using the following data: tunnel radius $R_t = 1$ m, rock Young modulus $E = 20$ GPa, Poisson ratio $\nu = 0.3$, friction angle $\phi = 30^\circ$, cohesion $c = 5$ MPa and initial stresses $\sigma_v = \sigma_h = 30$ MPa. Several values of normalized distances between the twin tunnels axes $d_1/2R_t$ have been investigated, and the configuration of single tunnel may be viewed as the limiting case $d_1/2R_t \gg 1$. These simulations also utilized symmetry concerning the midplane between the twin tunnels. It can be seen that the effect on the convergence of the roof is more pronounced when $d_1/2R_t$ is smaller than 2.

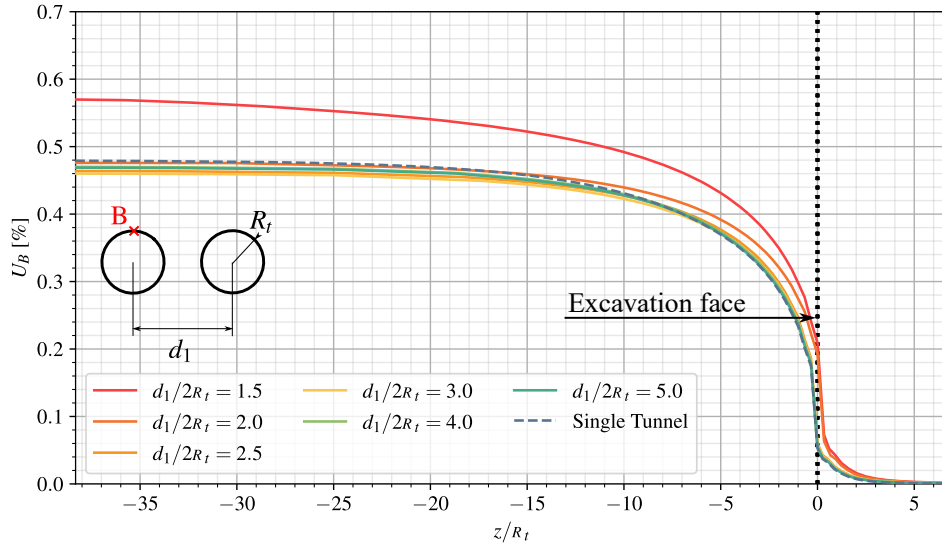


Figure 17: Convergence profiles in the tunnel roof (point B).

The tunnel deformation anisotropy induced by the twin tunnels proximity is illustrated in Fig. 18, which plots the ratio $U_B/U_A = u_y(B)/u_x(A)$ between the vertical displacement u_y at the roof B and the horizontal displacement u_x at the side wall A ($x = R_t, y = 0, z$). The results refer to a tunnel section located far behind the facing at normalized distance $z/R_t = -35$. They emphasize the significant tunnel ovalization induced by the proximity of twin tunnel as the distance $d_1/2R_t$ decreases. In this case, the horizontal displacement in the tunnel side wall in A is greater than the vertical displacement in the tunnel roof in B, indicating an ovalization along the tunnel's vertical axis.

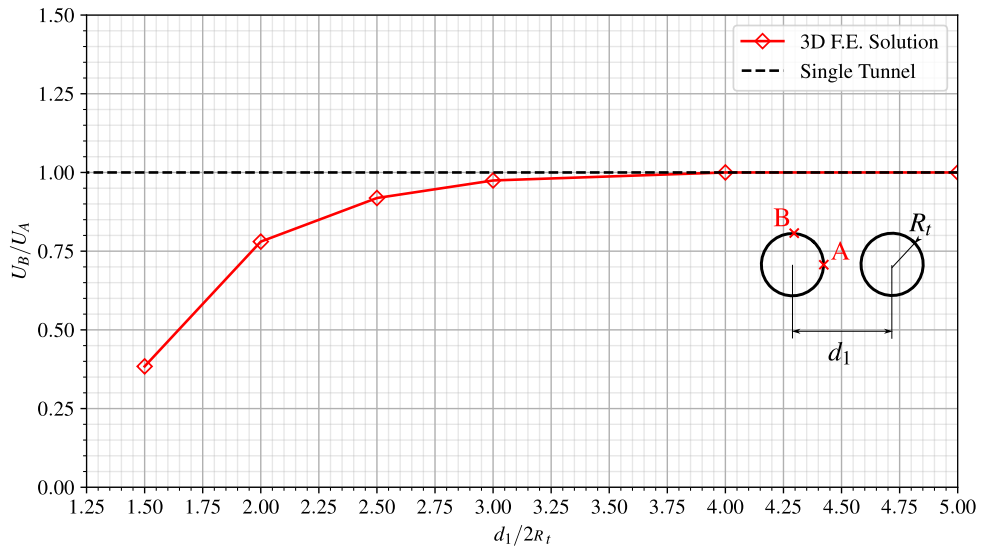


Figure 18: Illustration of the tunnel wall deformation anisotropy induced by twin tunnels proximity.

Fig. 19 shows the comparison between the 3D F.E. Solution (from a far behind the excavation face) and the analytical solution for plastic zone boundary provided in [9]. For these analysis, $R_t = 1$ m, $d_1/2R_t = 2.5$, Young's

modulus $E = 20$ GPa, Poisson's ratio $\nu = 0.3$ and, friction angle $\phi = 30^\circ$. The boundary of the plastic zone agrees very well with the elements that have reached the plasticity criterion.

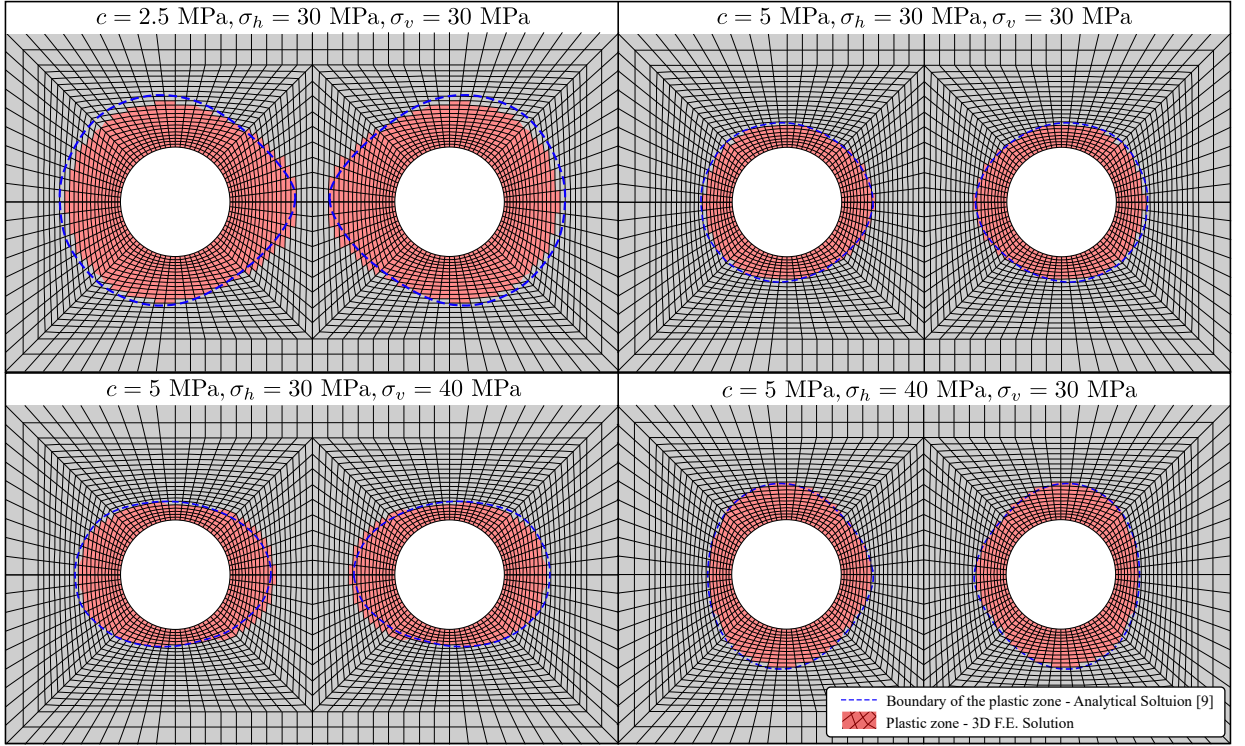


Figure 19: Comparisons between the numerical and analytical solution for the plastic zones considering $d_1/2R_t = 2.5$ and $\phi = 30^\circ$ for different initial conditions and cohesion values.

The stresses obtained in the 3D numerical simulation are compared quantitatively in Fig. 20 with the stresses derived from the elastoplastic analytical solution in [9]. This figure shows the radial and orthoradial stresses in polar coordinates (r, θ) considering three paths $\theta = 45^\circ, 90^\circ$ and 135° . Although the criterion adopted for numerical simulation is the Drucker-Prager inscribed in Mohr-Coulomb, the solution agrees very well with the analytical solution in the plastic zone.

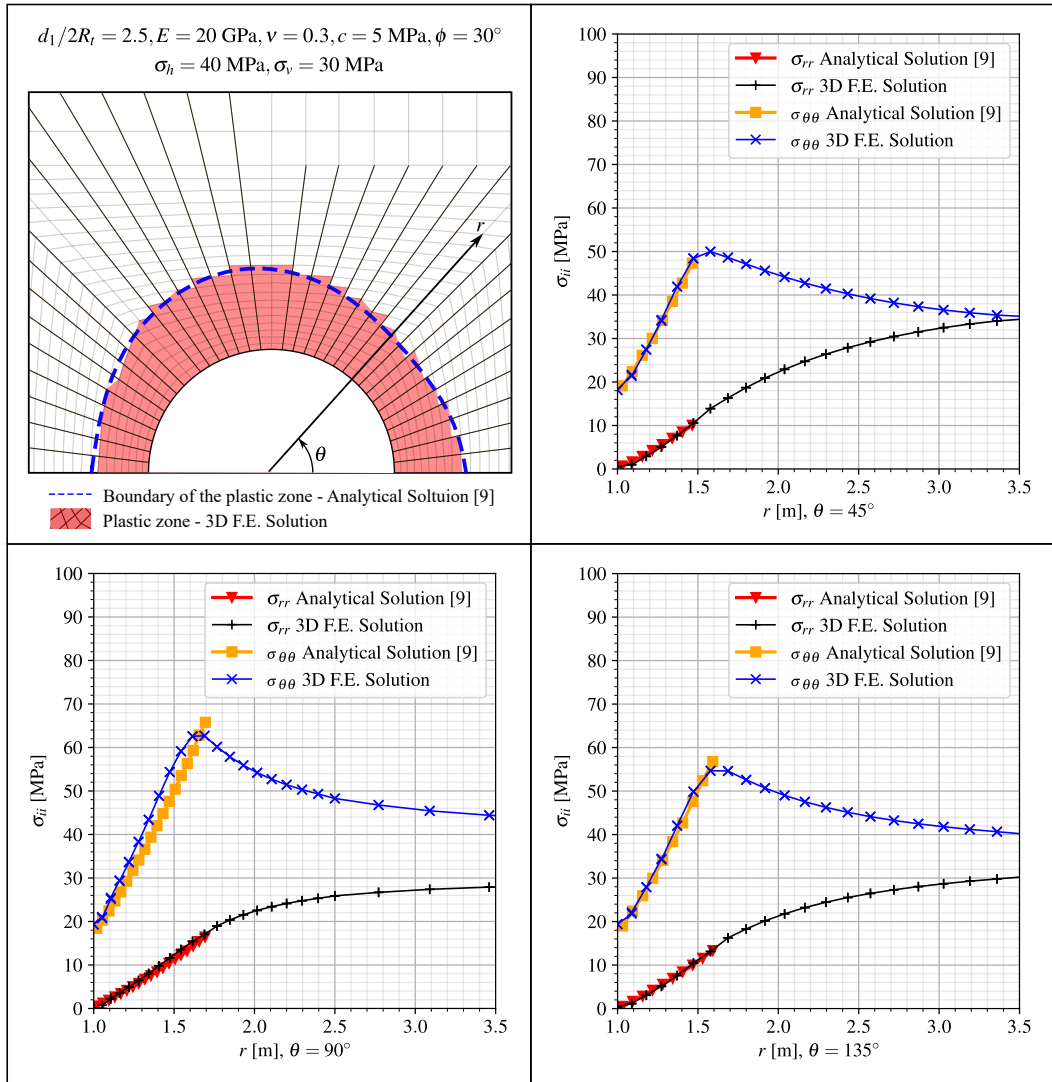


Figure 20: Comparisons between the numerical and analytical solution for different stress-paths.

As part of the study of mesh convergence, Fig. 21 shows the magnitude of the displacements u and stresses σ_{rr} , $\sigma_{\theta\theta}$ and σ_{zz} at element level in the gallery region for the case with $R_t = 1 \text{ m}$, $d_1/2R_t = 2.5$, $E = 20 \text{ GPa}$, $\nu = 0.3$, $c = 5 \text{ MPa}$, $\phi = 30^\circ$ and $\sigma_h = \sigma_v = 30 \text{ MPa}$. The smoothness observed in the solution between the elements indicates satisfactory spatial discretization.

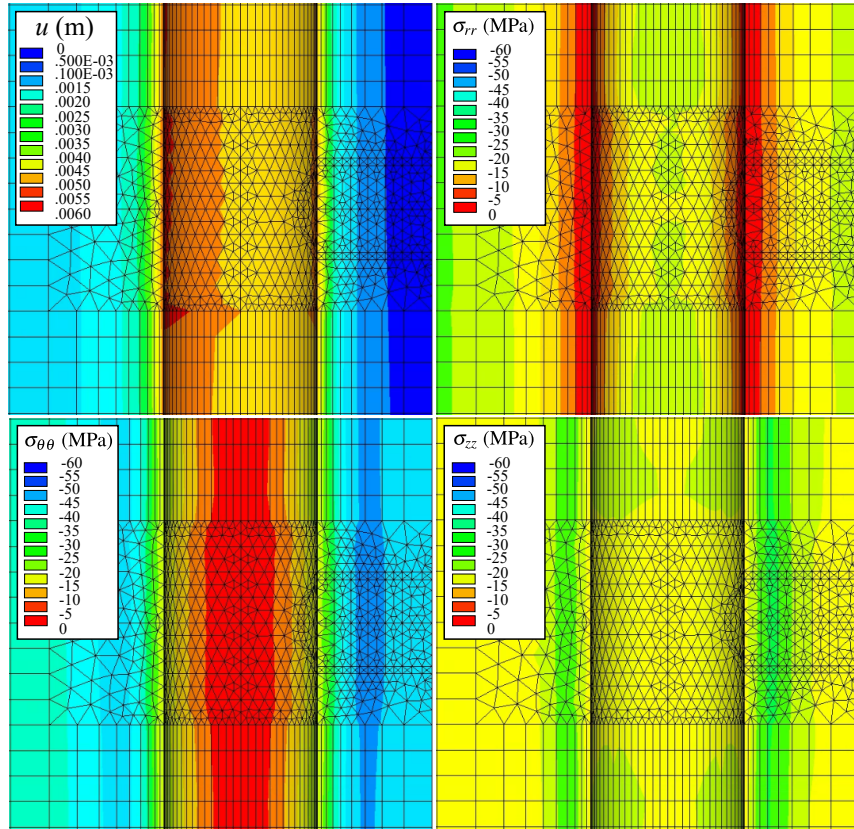


Figure 21: Element solution with $c = 5$ MPa, $d_1 = 5$ m, $\sigma_v = \sigma_h = 30$ MPa at the junction of the longitudinal tunnel with the gallery from the viewpoint of the symmetry plane $y = 0$

7. Numerical Results and Discussion

To develop the parametric analyses, we employed the constitutive parameters of the clay rock mass in the Paris basin (specifically in Aisne), as detailed in Piepi [22] and Rousset [18]. These parameters, shown in Table 2, were derived qualitatively from various axisymmetric triaxial compression tests, including cyclic and creep tests conducted under undrained conditions. Previous research by Giraud [20] indicates that for Aisne clay rocks, characterized by low porosity (typically less than 20%), hydromechanical coupling has minimal significance. The delayed effects primarily stem from material viscosity, with a low proportion attributable to pore pressure redistribution (hydraulic diffusion). The material exhibits high density (ranging from 2.01 to 2.57) and a low average water content (between 3 to 11%). Another characteristic is that irreversible deformations are observed in cyclic tests even at very small values of axial deformation (less than 0.3%). Furthermore, for confinement values exceeding 10 MPa (approximately the in situ confinement), the maximum deviation remains practically constant, suggesting a Tresca-type failure criterion.

During creep tests on this material, it was observed that creep deformations are of comparable magnitude to deformations observed during instantaneous tests, and there exists a deviatoric stress threshold beyond which creep phenomena initiate. Moreover, it was found that the influence of confining pressure on creep phenomena can be disregarded. Comparing both behaviors—instantaneous and delayed—reveals that short-term cohesion exceeds long-term cohesion, with the ratio between these two cohesion values ranging between 1.2 and 2.

For the lining, we employed typical values for ordinary reinforced concrete.

These parameters are shown in Table 2. In these analyses the radius is $R_l = 1$ m and excavation speed is 12.5 m/day.